GLIA

WILEY

RESEARCH ARTICLE

Neuroinflammatory reactive astrocyte formation correlates with adverse outcomes in perinatal white matter injury

Patricia Renz [1,2,3] | Marel Steinfort [1,2,3] | Valérie Haesler [1,2] |
Vera Tscherrig [1,2,3] | Eric J. Huang [4] | Manideep Chavali [5] |
Shane Liddelow [6,7,8] | David H. Rowitch [9,10,11,12] | Daniel Surbek [1,2] |
Andreina Schoeberlein [1,2] | Amanda Brosius Lutz [1,2]

[1]Department of Obstetrics and Gynecology, Division of Feto-Maternal Medicine, Inselspital, Bern University Hospital, University of Bern, Bern, Switzerland

[2]Department for BioMedical Research, University of Bern, Bern, Switzerland

[3]Graduate School for Cellular and Biomedical Sciences, University of Bern, Bern, Switzerland

[4]Department of Pathology, UCSF, San Francisco, California, USA

[5]Department of Pediatrics and Papé Family Pediatric Research Institute, Oregon Health and Science University, Oregon, USA

[6]Neuroscience Institute, NYU Grossman School of Medicine, New York, New York, USA

[7]Department of Neuroscience and Physiology, NYU Grossman School of Medicine, New York, New York, USA

[8]Department of Ophthalmology, NYU Grossman School of Medicine, New York, New York, USA

[9]Department of Pediatrics, UCSF, San Francisco, California, USA

[10]Eli and Edythe Broad Institute for Stem Cell Research and Regeneration Medicine, UCSF, San Francisco, California, USA

[11]Newborn Brain Research Institute, UCSF, San Francisco, California, USA

[12]Department of Paediatrics and Wellcome-MRC Cambridge Stem Cell Institute, University of Cambridge, Cambridge, UK

Correspondence
Amanda Brosius Lutz, Department of Obstetrics and Gynecology, Inselspital, Friedbühlstrasse 19, 3010 Bern, Switzerland.
Email: amanda.brosiuslutz@insel.ch

Abstract

Perinatal white matter injury (WMI) is the leading cause of long-term neurological morbidity in infants born preterm. Neuroinflammation during a critical window of early brain development plays a key role in WMI disease pathogenesis. The mechanisms linking inflammation with the long-term myelination failure that characterizes WMI, however, remain unknown. Here, we investigate the role of astrocyte reactivity in WMI. In an experimental mouse model of WMI, we demonstrate that WMI disease outcomes are improved in mutant mice lacking secretion of inflammatory molecules TNF-α, IL-1α, and C1q known, in addition to other roles, to induce the formation of a neuroinflammatory reactive astrocyte substate. We show that astrocytes express molecular signatures of the neuroinflammatory reactive astrocyte substate in both our WMI mouse model and human tissue affected by WMI, and that this gene expression pattern is dampened in injured mutant mice. Our data provide evidence that a neuroinflammatory reactive astrocyte substate correlates with adverse WMI disease outcomes, thus highlighting the need for further investigation of these cells as potential causal players in WMI pathology.

1 | INTRODUCTION

Perinatal white matter injury (WMI) is the most common cause of long-term neurological morbidity in infants born preterm (Volpe, 2019). Resulting from a series of inflammatory and hypoxic–ischemic insults to the developing brain during a window of oligodendrocyte lineage vulnerability between the 23rd and 32nd week of human gestation, WMI is characterized histologically by morphological "reactivity" changes in astrocytes and microglia and by myelination defects in periventricular white matter (Back, 2017; Volpe, 2019). Clinically, patients present with a broad spectrum of motor and cognitive deficits (Volpe, 2019). Treatment options are currently extremely limited, in large part hampered by a limited understanding of underlying disease pathophysiology (Eggenberger et al., 2019; Thomi et al., 2019; Volpe, 2019).

The molecular nature and role of astrocyte reactivity in WMI are currently unclear (Nobuta et al., 2012; Shiow et al., 2017; Srivastava et al., 2020). In light of recent progress highlighting the impressive diversity of astrocytes in the healthy and diseased brain, it is plausible that multiple reactive astrocyte substates with diverse contributions to disease outcomes form in brains affected by WMI (Ben Haim & Rowitch, 2017; Brandebura et al., 2023; Khakh & Sofroniew, 2015; Wheeler et al., 2019). Deciphering these reactive astrocyte substates and their roles in WMI is crucial to improving our mechanistic understanding of the disease and to enabling the discovery of more successful therapeutics.

Bulk sequencing experiments have demonstrated that after neuroinflammatory insults, such as exposure to the bacterial endotoxin lipopolysaccharide (LPS), astrocytes upregulate genes related to immune signaling, including cytokines and components of the complement cascade (Liddelow et al., 2017; Zamanian et al., 2012). These bulk gene expression changes can be grossly reproduced and abrogated in vitro and in vivo through exposure to and withdrawal of microglia-derived TNF-α, IL-1α, and C1q (Liddelow et al., 2017). Functional characterization of this neuroinflammatory reactive astrocyte substate shows that these cells lose many normal physiological astrocyte functions (e.g., synapse formation, phagocytosis, glutamate reuptake) (Liddelow et al., 2017). In addition, these cells are reported to be toxic to neurons and mature oligodendrocytes and to block OPC-to-oligodendrocyte differentiation in culture (Guttenplan et al., 2021; Liddelow et al., 2017) Prevention of astrocyte conversion to the neuroinflammatory reactive substate has been shown to improve disease outcomes in rodent models of several adult neurodegenerative diseases, including Amyotrophic Lateral Sclerosis (ALS), glaucoma, and Parkinson's disease (Brandebura et al., 2023; Guttenplan, Stafford et al., 2020; Guttenplan, Weigel et al., 2020; Yun et al., 2018). Based on this data, we hypothesized that neuroinflammatory reactive astrocytes form in WMI and play a causal role in WMI pathology.

2 | METHODS

2.1 | Animals

All animal procedures were approved by the Veterinary Department of the Canton of Bern, Switzerland (reference number: BE19/85) and kept under standard housing conditions. We used C57BL/6 wildtype (WT; B6.Tg(Aldh1l1–eGFP)<OFC789Gsat>/Mmucd) and triple knockout (TKO; B6.Cg-Il1a<tm1Yiw>Tnf<tm1Gkl>C1qa<tm1Barr>Tg(Aldh1l1–eGFP)<OFC789Gsat>/Barr) mice. TKO mice were a gift from SL.

2.2 | Mouse model of perinatal WMI

The two-hit acute diffuse perinatal WMI was induced, according to Renz et al. (2022). Briefly, mice were randomly assignment to an injured or an uninjured group. In the injury group, mouse pups were injected subcutaneously between the scapulae with 2 mg/kg (0.2 μg/μL, approximate inoculate volume 15–20 μL) body weight (BW) LPS (Escherichia coli strain O55:B5, Sigma Aldrich) on postnatal day (P)2, placed on an isolette and submitted to a hypoxic insult (8% O_2/92% N_2, 3 L/min) for 25 min 6 h after LPS injection. Uninjured mice received an equivalent volume of saline and were placed for 25 min 6 h after saline injection in a temperature-controlled, normoxic environment. Neonatal mortality is observed during or directly after hypoxia in 20%–30% of mouse pups.

2.3 | Immunohistochemistry on mouse tissue

2.3.1 | Myelin basic protein

At 9 days after injury (9 dpi), injured and uninjured WT and TKO mice were terminally anesthetized and perfused transcardially with phosphate-buffered saline (PBS) followed by 4% paraformaldehyde (PFA). Brains were removed and fixed in 4% PFA for 24 h at 4°C. After fixation, all brains were embedded in paraffin and 6 μm sections in the coronal plane at the level of the hippocampus were cut using a microtome. Prior to staining, sections were deparaffinized and rehydrated. After antigen retrieval in 0.1 M sodium citrate buffer in a pressure cooker for 12 min, sections were washed in 1× tris-buffered saline (TBS) with 0.1% Tween 20 (Sigma Aldrich) and blocked for 1 h at room temperature (RT) with 10% goat serum, 1% bovine serum albumin (BSA, Sigma Aldrich) in TBS. Sections were then incubated overnight at 4°C with the polyclonal rabbit anti-myelin basic protein (MBP) antibody (1:200, ab40390, Abcam) diluted in blocking buffer. Sections were next washed three times in 1× TBS and incubated with the secondary antibody (Alexa fluor® 488-conjugated goat anti-rabbit IgG, Invitrogen, a11008, 1:200) for 1 h at RT in the dark. Sections were counterstained with DAPI (Sigma Aldrich).

2.3.2 | Cux1/2

Protocol as described above for MBP with the following changes. Antigen retrieval performed in Tris-EDTA (TE) buffer pH 8.5. Primary Antibody: Rabbit anti-Cux1 and Cux2 (Abcam ab309139, 1:500). Secondary Antibody: Alexa fluor 594-conjugated goat anti-rabbit IgG (Invitrogen A32740, 1:200).

2.3.3 | Cux1/2, TUNEL double IHC

Injured and uninjured WT and TKO mice were euthanized using rapid decapitation 24 h after injury. Brains were removed and directly fixed through immersion in 4% PFA for 24 h at 4°C. Paraffin embedding and sectioning as described above. Antigen retrieval with TE Buffer pH 8.5. Tissue was permeabilized with 0.1% Triton X-100 in PBS prior to blocking with 10% goat serum, 1% BSA. Following Blocking, TUNEL staining was performed using the In Situ Cell Death Detection Kit, Fluorescein (Roche 11684795910) for 1 h at 37°C according to the manufacturer's instructions. Subsequent primary and secondary antibody incubation as described above.

2.3.4 | Iba1

Preparation of paraffin-embedded brain slices 24 h after injury as described above. Primary antibody incubation overnight at 4° with rabbit anti-Iba1 (abcam 178846, 1:2000). For DAB staining, signal amplification with goat anti-rabbit HRP secondary antibody (DAKO, P0448, 1:100), followed by application of DAB chromogen substrate.

2.3.5 | GFP

Preparation of paraffin-embedded brain slices 24 h after injury as described above. Primary antibody incubation overnight at 4° with rabbit anti-GFP (Abcam ab290, 1:750). Fluorescence and DAB labeling as described above.

2.4 | RNAscope® in situ hybridization

C3: RNAscope® fluorescent in situ hybridization was performed on paraffin embedded brain sections. Mice pups 1 day postinjury (1 dpi) and 2 days postinjury (2 dpi) were euthanized using rapid decapitation. Brains were removed and directly fixed in 4% PFA for 20 h at 4°C and embedded in paraffin. Nine dpi tissue was obtained as described in the immunohistochemistry methods. RNAscope® Multiplex Fluorescent Reagent Kit v2 (Cat. Nr. 323110, Advanced Cell Diagnostics (ACDbio)) was used according to the manufacturer's protocol. Specific probes for *C3* (Cat. Nr. 417848, ACDbio), *Gfap* (Cat. Nr. 313211-C2, ACDbio), and *Aldh1l1* (Cat. Nr. 405891-C2, ACDbio) were used. The astrocyte-specific probes *Gfap* and *Aldh1l1* were mixed 1:1 (astrocyte probe mix). Probes were detected using Opal dye 570 (FP1488001KT, Akoya Biosciences) for *C3* and Opal dye 520 (FP1487001KT) for the astrocyte probe mix. In addition, after RNAscope detection of *C3* some slides were colabeled with an anti-GFAP antibody (1:400, mab360, Millipore) according to the immuno-histochemistry/ISH double labeling protocol provided by ACDbio.

For *C1s* and *Psmb8* ISH probes, labeling was performed using fresh frozen tissue. Injured and uninjured WT and TKO mice were euthanized using rapid decapitation 24 h after injury. Brains were rapidly removed, submerged in OCT, and flash frozen in liquid nitrogen. Tissue was stored at −80°C until further use. 14 μm cryosections were prepared at −20°C. Slides were returned to −80°C until use. Upon removal from −80°C, slides were immediately fixed in ice cold 4% PFA for 90 min. Further tissue processing was performed according to the RNAscope Multiplex Fluorescent Reagent Kit v2, as described above. Tissue was pretreated with Protease 3 for 22 min. Specific probes: C1s (Mm-C1s, Cat. 479961 Nr., ACDbio), Psmb8 (Mm-Psmb8Cat. Nr. 434241, ACDbio). In addition to *Gfap* and *Aldh1L1*, astrocyte marker *GLAST* (Mm-Slc1a3, Cat. Nr. 430781-C2, ACDbio) was added to the astrocyte probe mix (Probes mixed 1:1:1).

2.5 | Image analysis

All image analysis was performed blinded. Images were either scanned on a Panoramic 250 Flash II slide scanner (3DHISTECH) or acquired with a DM6000 B microscope (Leica Microsystems) or a laser scanning confocal microscope (Carl Zeiss LSM 710). MBP, GFP (Aldh1L1), and Iba1 immunohistochemistry was quantified using ImageJ Software v1.47 (Rasband, W.S., National Institutes of Health, Bethesda, MD, USA, http://imagej.nih.gov/ij). For percent signal positive area calculations, a user-defined supervised macro was used to quantify the MBP positive signal area within the regions of interest (corpus callosum or cortex) that was above a defined signal intensity threshold as a percentage of the defined area. For cell body fraction calculations (Iba1), a supervised user-defined macro was again used involving two consecutive signal quantifications, one at a threshold resulting in labeling of cell body and cell processes and a second quantification at a higher threshold leaving only cell somas labeled. The fraction of these two measurements was reported. For quantification of Cux1 and 2 positive cortical layer density, the antibody-labeled region was selected and a user-defined macro was used to automate counting of labeled nuclei. Nuclei counts were divided by the area of the region examined.

2.6 | Rotarod

Motor coordination and balance were tested in injured and healthy WT and TKO mice at 28 days postinjury (28 dpi) using the rotarod. The rotarod test was performed as in Renz et al. (2022). Briefly, on the first day, the mice were trained to remain on the wheel at 5 rpm for 5 min. The next day, the rotational speed was continuously increased from 15 to 33 rotations/min (rpm), alternating between forward and backward rotation over 5 min. The mean latency to fall across three trials was recorded.

2.7 | Novel object recognition

Recognition memory was assessed at 28 dpi using the novel object recognition task. Briefly, the animals were habituated to the open field

1 day before the task. On the following day, mice were returned to the same open field containing two identical objects. Four hours later, the mice explored the open field again in the presence of one familiar object and one new object (novel object). The order of object presentation and the relative object positions was randomized between mice. Total object exploration time was limited to 20 s with a maximum of 10 min in the open field. All animals met the 20 s exploration limit prior to 10 min in the open field. It follows that total object exploration time was equal for all animals in order to avoid potential bias due to motor impairment. The discrimination ratio was calculated as novel object interaction time/total object interaction time with both objects.

2.8 | Preparation of live brain cell suspensions and fluorescence-activated cell sorting isolation of astrocytes

Live single-cell suspensions from a single healthy and injured mouse brain 1 day after injury (1 dpi) were prepared as follows: cortices and underlying white matter were enzymatically digested using papain and then mechanically dissociated to yield a single cell suspension according to the immunopanning protocol of (Foo et al., 2011). The cells were resuspended in Dulbecco's PBS (DPBS) containing 0.02% BSA and 125 U/mL DNase, filtered through a nitex mesh filter (Tetko HC3-20) and supplemented with 1 μg/mL propidium iodide (PI) for fluorescence-activated cell sorting (FACS) (Zamanian et al., 2012). Subsequently, astrocytes were sorted at 4°C using BD FACS ARIA III for GFP fluorescence in the absence of PI to select live astrocytes at the Flow Cytometry and Cell Sorting Facility (FCCS) of the Department for BioMedical Research, University of Bern, Switzerland.

2.9 | mRNA isolation and microfluidic qRT-PCR

Total RNA was isolated from FACS-purified astrocytes from a single mouse brain using the QIAshredder and the All-prep DNA/RNA/protein Mini Kit according to the manufacturer's protocol (Qiagen). Total RNA concentration was measured using a NanoVue PlusTM spectrophotometer (Biochrom). Microfluidic qRT-PCR was performed using the Biomark HD System from Fluidigm according to the manufacturer's protocol using the Delta Gene™ Assay and a 96.96 Dynamic Array™ IFC for Gene Expression. Briefly, cDNA was prepared using the reverse transcriptome master mix (PN 100-6297) followed by preamplification with the Preamp Master Mix (PN 100-5580) using the GE Fast 96 × 96 PCR + Melt v2 thermal cycling protocol according to the manufacturer's instructions (Standard Biotools). The 96.96 Dynamic Array™ IFC was primed (including diluter cDNA and primer mastermix) using the Biomark HX system IFC Controller. The loaded chip was processed in the Biomark HD Real-Time PCR System (Standard Biotools) and cycled as follows: 10 min at 95°C followed by 40 cycles of 95°C for 15 s, 60°C for 30 s and 72°C for 30 s. Data were collected and quantified using BioMark Data Collection

Software 2.1.1 build 20090519.0926 from Standard Biotools. Expression data for each sample were normalized to the sample mean of *Rplp0* and *Aldh1l1* expression (Table S4). Fold change for each gene was calculated relative to the mean expression of the corresponding gene in uninjured samples.

2.10 | Human postmortem neonatal brain specimens

Human postmortem fixed-frozen brain tissue samples obtained from University of California, San Francisco's Pediatric Neuropathology Research Laboratory were used for this study. All human tissue were collected in accordance with guidelines established by the University of California, San Francisco Committee on Human Research (H11170-19113-07) following the provision of informed consent. The procurement of deidentified postmortem human brain tissues was approved by the Institutional Review Board at the University of California San Francisco (#12-08643).Human postmortem tissue was fixed with 4% PFA and subsequently cryopreserved sequentially in 10%, 20%, and 30% sucrose. Frozen tissue was then cut into 14 μm sections for further examination. WMI was diagnosed by an experienced neuropathologist by the presence of astrogliosis and macrophage infiltration. Tissue from infants that died as a consequence of VATER malformations was used as a control. WMI and control cases were matched as closely as possible based on gestational age at the time of birth, postnatal age at the time of death and brain region.

2.11 | Staining of human postmortem tissue

In situ hybridization combined with immunohistochemistry was performed on fixed-frozen postmortem brain sections using the the RNAscope® Multiplex Fluorescent Reagent Kit v2 (Cat. Nr. 323135, ACDbio). Briefly, sections were prepared as follows: washed in PBS for 5 min, baked at 60°C for 30 min, fixed in 4% PFA on ice, dehydrated in 50%, 70%, and 100% ethanol for 5 min at RT and then airdried. After hydrogen peroxide treatment for 10 min at RT, the target retrieval was performed for 5 min at 95°C. Subsequently, sections were treated with Protease III for 10 min at 40°C. The hybridization using probe *C3* (Cat. Nr. 430701-C3, ACDbio) and all further amplification steps were performed according to the manufacturer's protocol. After the detection step using Opal dye 570 (SKU FP1488001KT, Akoya Biosciences), sections were washed in RNAscope® wash buffer and blocked in 5% horse serum, 0.2% Triton X-100 (Sigma Aldrich) in 1× PBS for 1 h at RT. Subsequently, sections were incubated overnight at 4°C with the primary anti-GFAP antibody (1:400, G3893, Sigma Aldrich). Next, sections were incubated with the secondary antibody (Alexa fluor® 488-conjugated, Thermo Fisher Scientific) for 1 h at RT and counterstained with DAPI for 30 s. All tissue sections were scanned using the Panoramic 250 Flash II slide scanner for quantification. All data analysis was performed blinded. The percentage of GFAP positive astrocytes labeled with *C3* was counted in 3–6 evenly

spaced circular regions (0.5 mm²) placed across the white matter region of interest. GFAP expressing cells showing more than five *C3* RNAScope® fluorescence probe spots were counted as positive.

2.12 | Statistical analysis

After passing tests for normality (Kolmogorov–Smirnov test or Shapiro–Wilk test), data were analyzed using one-way ANOVA (multiple comparisons between WT/TKO injured/uninjured) or student's *t*-test (time course of C3 expression, Quantitative reverse transcription polymerase chain reaction (qRT-PCR)). Significance was determined at $p < .05$.

3 | RESULTS

3.1 | Knockout of *Tnf*, *Il1a*, and *C1q* improves myelination and functional outcomes in an experimental acute perinatal WMI model

Work in recent years has demonstrated that neuroinflammatory reactive astrocytes form in response to simultaneous expression of several microglial derived factors, namely *Tnf*, *Il1a*, and *C1q* (Liddelow et al., 2017). Silencing of one or more of these genes prevents neuroinflammatory reactive astrocyte formation and improves disease outcomes in rodent models of multiple adult neurodegenerative diseases (Brandebura et al., 2023; Guttenplan, Stafford et al., 2020; Guttenplan, Weigel et al., 2020; Yun et al., 2018). Based on these findings, we first aimed to examine the effect of silencing *Tnf*, *Il1a*, and *C1q* on WMI outcomes during early development. To ask this question, we used a multihit inflammatory/hypoxic mouse model of acute diffuse perinatal WMI recently published by our group and *Tnf*, *Il1a*, *C1q* global TKO

mice. Our mouse model recapitulates key features of human disease including reactive changes in microglia and astrocytes, maturation defects in the oligodendrocyte lineage, myelination failure, and motor and cognitive deficits (Renz et al., 2022). TKO mice develop and reproduce normally. We began by quantifying myelination in the corpus callosum at postnatal day 11 (9 days postinjury, dpi) in TKO mice in comparison with WT C57Bl/6 mice (Figure 1a). We observed the expected myelination defects in the corpus callosum of injured WT mice. This myelination defect was significantly reduced in injured TKO mice (Figure 1b). We did not observe a significant difference in myelination of the corpus callosum between uninjured WT and uninjured TKO mice (Figure S1).

Our rodent model of perinatal WMI also results in functional deficits that mirror the sensorimotor and cognitive disabilities observed in humans affected by WMI (Renz et al., 2022).Using rotarod and novel object recognition testing at 28 dpi, we observed the expected deficits in motor performance and recognition memory in injured compared with uninjured WT mice. These performance deficits were reduced in TKO mice (Figure 1c,d).

3.2 | Injury-induced morphologic reactivity changes in astrocytes and microglia are dampened in TKO mice

To begin to probe the mechanism(s) underlying improved myelination in TKO mice, we quantified astrocyte and microglia cell number and morphology as well as neuronal cell death at 24 h after injury in these mice, the timepoint at which maximal changes in these parameters were observed in our mouse model to date (Renz et al., 2022). Our quantification of astrocytes was performed in mice expressing GFP under the control of the promoter for astrocyte marker Aldh1L1. Our results did not show any significant differences in astrocyte or microglia number in the cortex or corpus
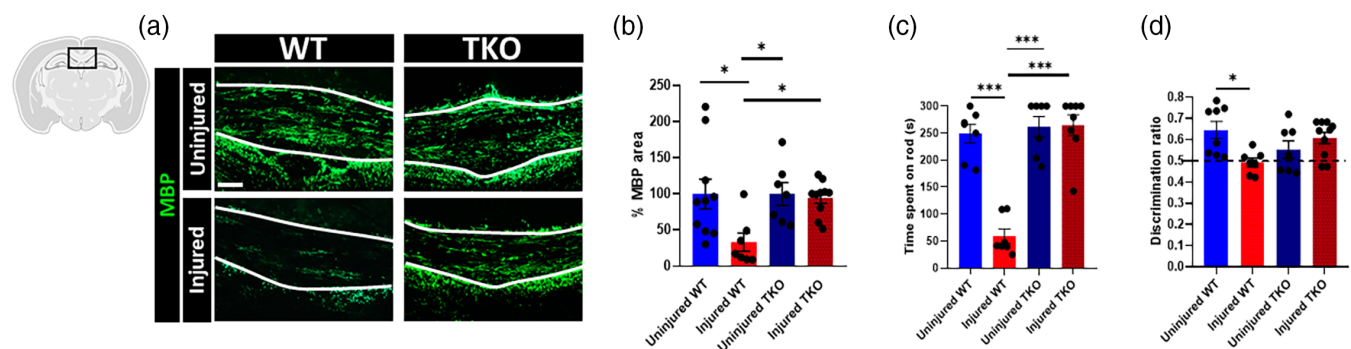

FIGURE 1 Quantification of myelination defects and behavioral outcomes after perinatal white matter injury in *Tnf*, *Il1a*, *C1q* triple knockout (TKO) and wildtype (WT) C57Bl/6mice. (a) Representative images of myelin basic protein immunofluorescence (IF) (green) in the medial corpus callosum of uninjured and injured WT and TKO mice at 9 days postinjury. Scale bar: 100 μm. (b) Quantification of myelin basic protein (MBP) immunofluorescence in the medial corpus callosum of uninjured and injured WT and TKO mice. Percentage areas were normalized to the mean % area of uninjured mice. Uninjured WT ($n = 10$), injured WT ($n = 7$), uninjured TKO ($n = 7$), and injured TKO ($n = 10$). (c) Quantification of rotarod (left) and novel object recognition (right) test performance. Uninjured WT ($n = 7$), injured WT ($n = 7$), uninjured TKO ($n = 7$), and injured TKO ($n = 8$). Data are presented as mean ± SE. *$p < .05$; **$p < .01$; ***$p < .001$. Difference is insignificant unless denoted with asterisk.
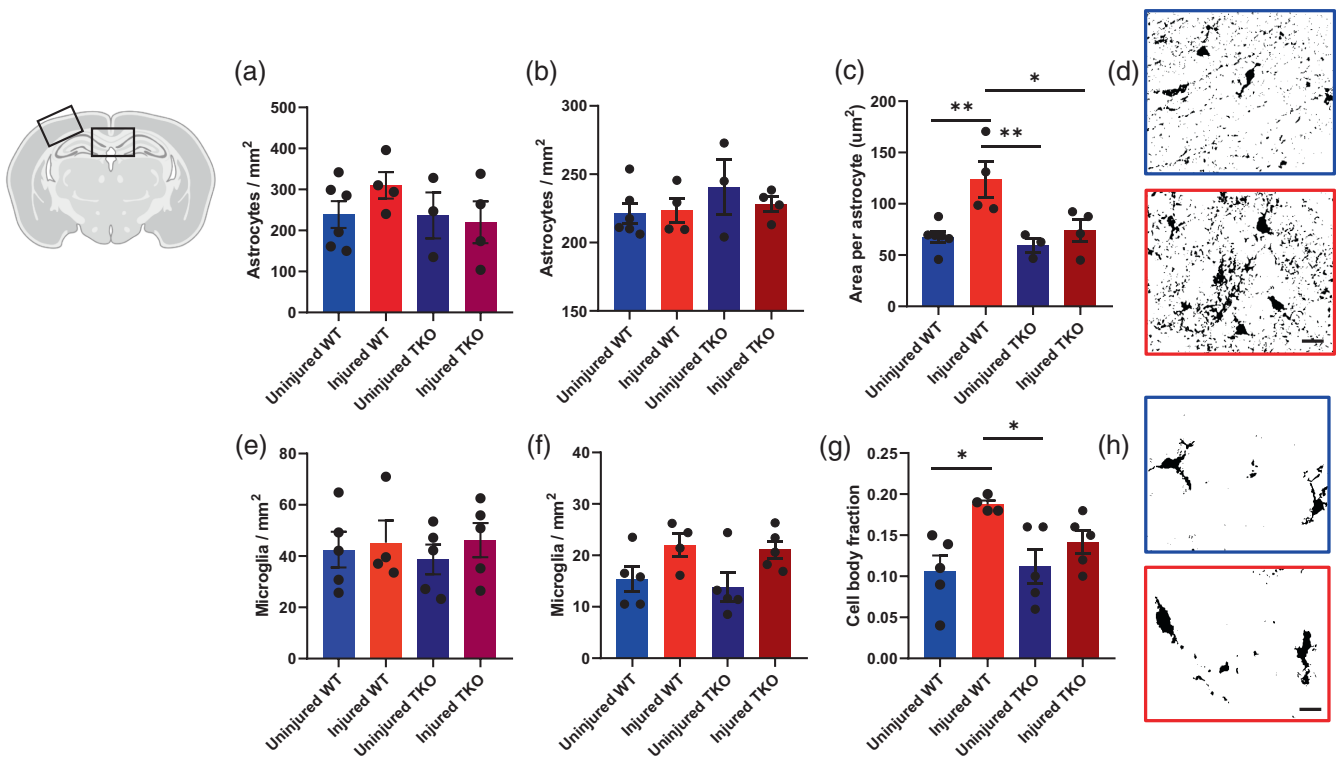
FIGURE 2 Characterization of astrocytes and microglia 24 h after injury in wildtype (WT) and triple knockout (TKO) mice. Quantification of GFP+ (experiment performed in Aldh1L1-GFP mice) astrocytes in the (a) corpus callosum and (b) cerebral cortex. (c) Quantification of area GFP + signal per cell in the cerebral cortex. (d) Representative pseudocolored DAB images of cortical astrocytes in uninjured (top) and injured (bottom) WT mice. Quantification of Iba1 + microglia in the (e) corpus callosum and (f) cerebral cortex. (g) Quantification of cell body fraction for Iba1 + microglia in the cerebral cortex. Representative pseudocolored DAB images of cortical microglia in uninjured (top) and injured (bottom) WT mice. Scale bar: 10 μm. Uninjured WT ($n = 6$), injured WT ($n = 4$), uninjured TKO ($n = 3$), and injured TKO ($n = 4$). Data are presented as mean ± SE. *$p < .05$; **$p < .01$; ***$p < .001$. Difference is insignificant unless denoted with asterisk.
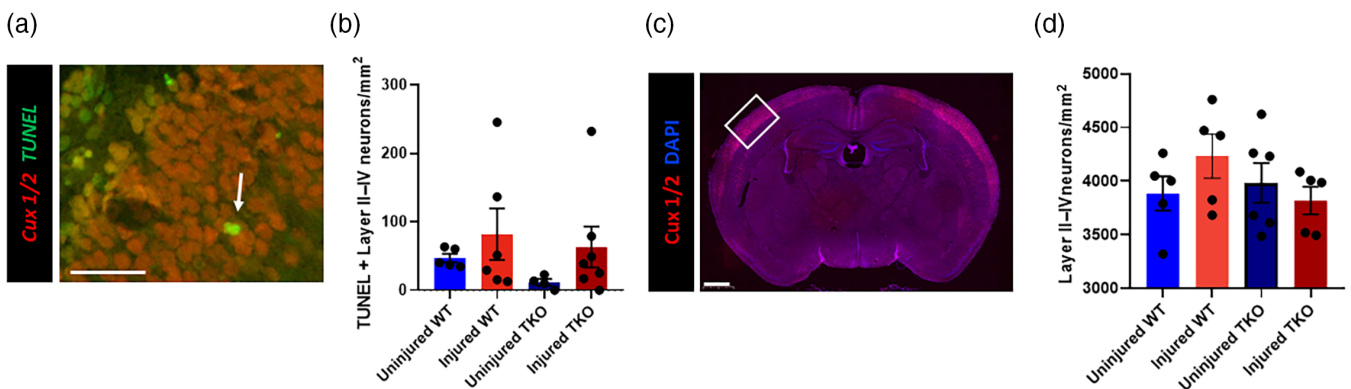

FIGURE 3 Quantifying neuronal death in cortical layers II–IV. (a) Immunohistochemistry of a postnatal day 3 brain labeled with TUNEL as a marker of cell death and Layer II–IV marker Cux1/2. Scale bar 25um. (b) Quantification of (a). (c) Quantification of neuronal density in Layers II–IV at postnatal day 11 evaluated using Cux1/2 immunostaining. Scale bar 1mm. Sample numbers at postnatal day 3: uninjured wildtype (WT) ($n = 5$), injured WT ($n = 6$), uninjured triple knockout (TKO) ($n = 4$), and injured TKO ($n = 7$). Sample numbers at postnatal day 11: uninjured WT ($n = 5$), injured WT ($n = 5$), uninjured TKO ($n = 6$), and injured TKO ($n = 5$). Data are presented as mean ± SE. *$p < .05$; **$p < .01$; ***$p < .001$. Difference is insignificant unless denoted with asterisk.

callosum regions at 24 h after injury between WT and TKO mice (Figure 2a,b,e,f). Nor did we observe significant baseline differences in the number or morphology of astrocytes or microglia between uninjured WT and TKO mice. Morphologically, both astrocytes and microglia in the cortex exhibit signs of reactivity following injury in WT mice. The signal area per astrocyte in the
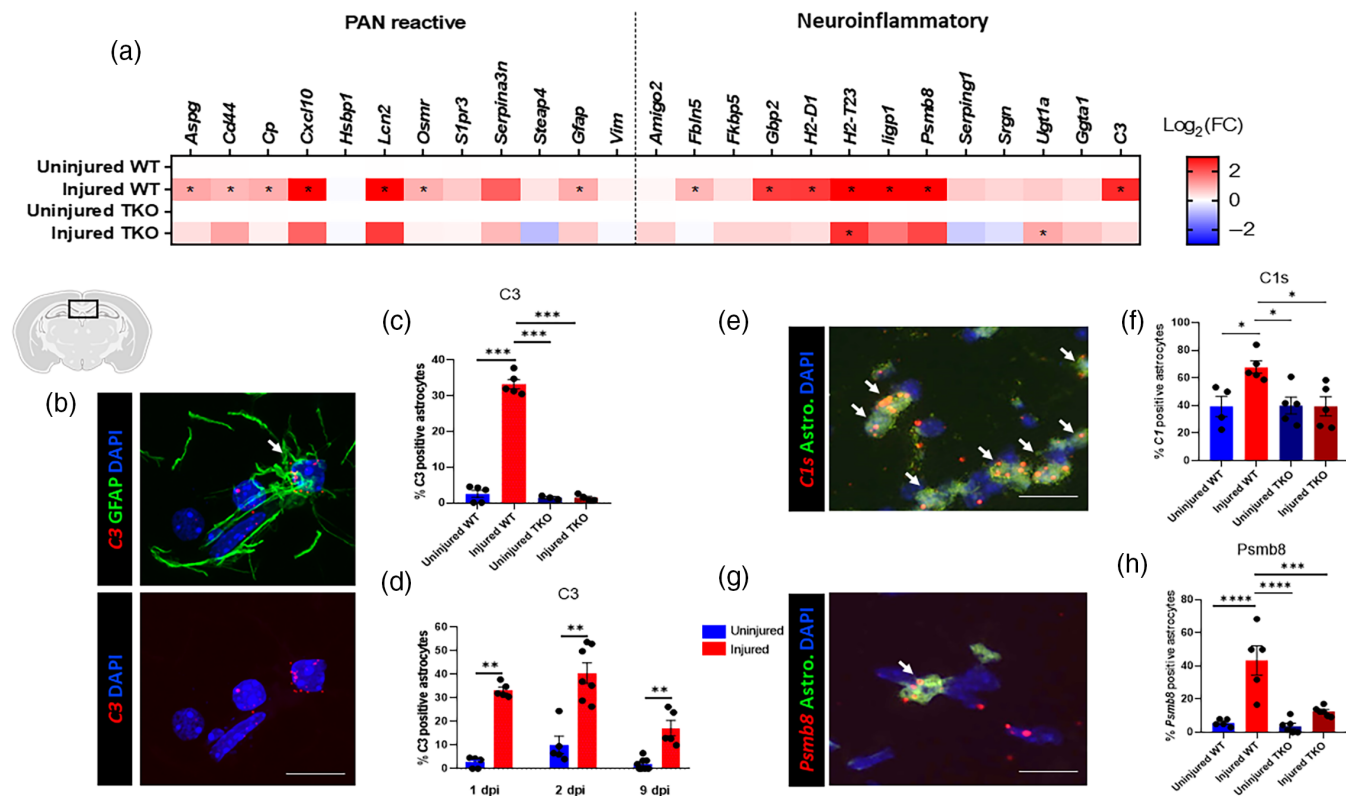
FIGURE 4 Formation of neuroinflammatory (C3+) astrocytes in rodent model of perinatal white matter injury in *Tnf, Il1a, C1q* triple knockout (TKO) and wildtype (WT) C57Bl/6 mice. (a) Microfluidic qRT-PCR for a panel of genes broadly upregulated in many reactive astrocyte substates ("PAN reactive"), and genes characteristic of the neurotoxic astrocyte response to neuroinflammation ("neuroinflammatory"). Heatmap compares the mean fold change (FC) of "PAN reactive" and neurotoxic neuroinflammatory gene transcripts from astrocytes isolated from the cortex and white matter of uninjured and injured WT ($n = 6$) or TKO ($n = 4$) mice. Data are normalized to mean values for uninjured WT and TKO mice. Exact p-values for the heatmap are listed in Table S3. (b) In situ hybridization for neuroinflammatory reactive astrocyte marker *C3* (red) and immunohistochemistry for GFAP (green) in the mouse corpus callosum of an injured WT brain. Scale bar: 10 μm. (c) Quantification of in situ hybridization for astrocyte markers *Aldh1l1* and *Gfap* (probe mix) and neuroinflammatory astrocyte marker *C3*. The graph depicts the percentage of astrocytes expressing *C3* in the corpus callosum at 1 dpi in WT ($n = 5$) and TKO ($n = 4$) injured and injured mice. (d) Time course of *C3*-expressing reactive astrocyte formation in injured and uninjured WT mice. Cells were quantified using in situ hybridization as in (b). The graph depicts the percentage of astrocytes expressing *C3* in the corpus callosum in uninjured (1 dpi: $n = 5$; 2 dpi: $n = 5$; 9 dpi: $n = 10$) and injured (1 dpi: $n = 5$; 2 dpi: $n = 7$; 9 dpi: $n = 7$) WT mice. (e, g) Representative image of corpus callosum from injured WT mouse labeled with in situ hybridization for astrocyte markers *Aldh1l1*, *Gfap*, and *Slc1a3* (probe mix) and neuroinflammatory astrocyte mRNA transcripts *C1s* (e) *and Psmb8* (g). *C1s* and *Psmb8* positive astrocytes are denoted with white arrows. Scale bar 25um (f, h) Quantification of in situ hybridization as in (b). The graph depicts the percentage of astrocytes expressing *C1s* or *Psmb8* in the corpus callosum at 1 dpi in WT ($n = 4$–5) and TKO ($n = 5$) uninjured and injured mice. Data are presented as mean ± SE. *$p < .05$, **$p < .01$, ***$p < .001$, ****$p < .0001$. Difference is insignificant unless denoted with asterisk.

cortex was significantly increased in WT mice (Figure 2c,d). Similarly, microglia appear more amoeboid and less ramified in the injured WT cortex, quantified using cell body fraction as an indicator of reactivity (Figure 2c,d,g,h). Neither of these morphological changes reached statistical significance in injured TKO mice.

Collosal axons originate primarily from layers II/III of the cortex. We therefore used Cux1 and 2, markers of cortical layers II–IV, combined with TUNEL labeling of cell death to quantify the death of neurons sending axons into the corpus callosum at postnatal day 3, 24 h after injury (Figure 3a,b). To assess persistent changes in layer III architecture, we also qualitatively and quantitatively assessed neuronal density in layers II–IV at

postnatal day 11 using Cux1 and 2 immunolabeling (Figure 3c,d). Neither of these methods revealed evidence for a significant increase in neuronal cell death in the cerebral cortex at the time-points examined.

3.3 | A C3-expressing neuroinflammatory reactive astrocyte substate forms in perinatal WMI and does not form in TKO mice

To more deeply understand changes in astrocytes induced by our WMI model, we examined the expression of genes broadly
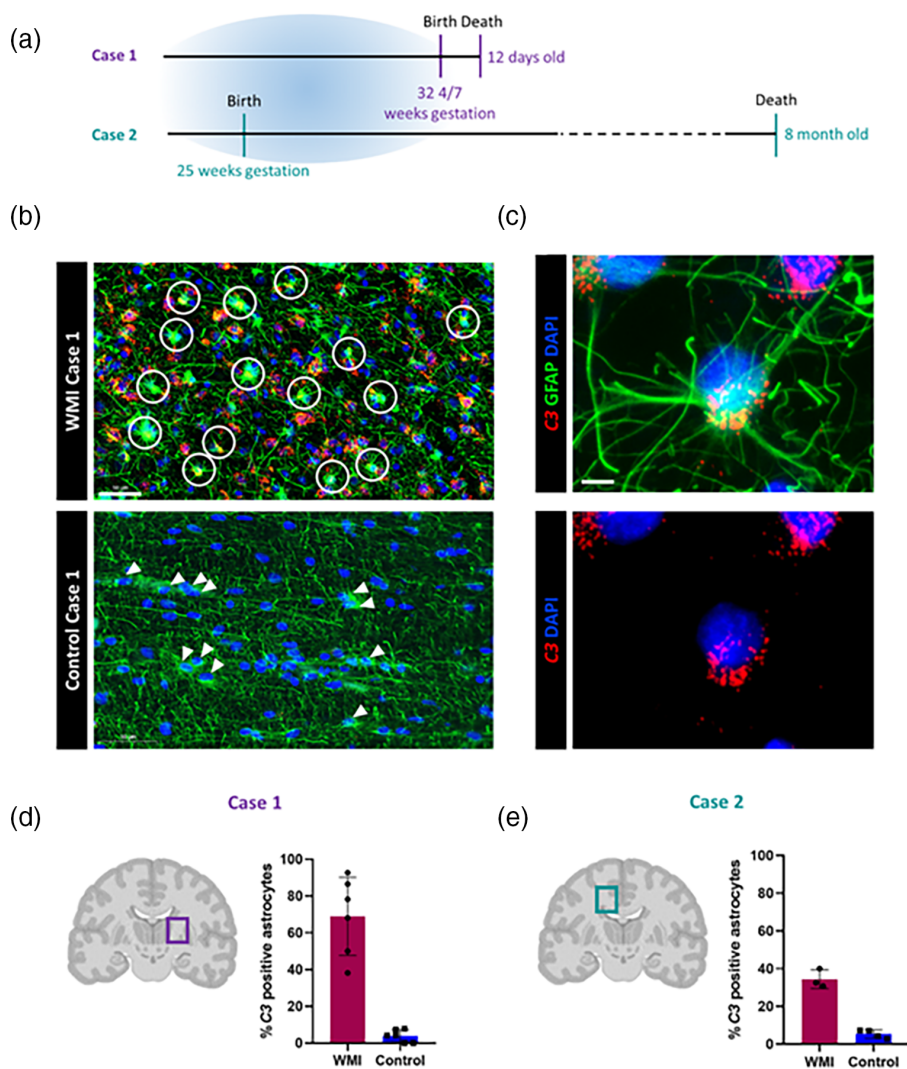
FIGURE 5 Formation of *C3*-expressing astrocytes in the human brain of perinatal white matter injury. (a) Timeline of gestational age at birth and postnatal age at time of death for white matter injury case 1 (purple) and case 2 (green). The blue area indicates the time window of pre-oligodendrocyte vulnerability. (b) Representative images of the human postmortem tissue of the WMI case 1 and Control case 1. White circles indicate astrocytes coexpressing *C3* (red) and GFAP (green) in WMI case 1. Arrowheads indicate astrocytes (green) in control case 1. Scale bar: 50 μm. (c) Confocal image of in situ hybridization for neurotoxic neuroinflammatory reactive astrocyte marker probe *C3* (red) and immunohistochemistry for GFAP (green) in the human WMI case 1. Scale bar: 10 μm. (d, e) Coronal brain sections indicating the brain region used for quantifying the percentage of astrocytes expressing marker *C3* in case 1 (d) and case 2 (e) in WMI and matched control cases. Data points represent the percent of astrocytes expressing *C3* in single 0.5 mm^2 circles spaced regularly throughout the anatomical region of interest.

associated with astrocyte reactivity (Liddelow et al., 2017; Zamanian et al., 2012). Using microfluidics qRT-PCR of FACS-purified astrocytes isolated from the cortex and underlying white matter of WT mice at 1 dpi, we demonstrated significant upregulation of numerous genes expressed across many reactive astrocyte substates (Guttenplan et al., 2021; Hasel et al., 2021; Zamanian et al., 2012). We refer these transcripts as "PAN reactive" genes and they include *Aspg*, *Cd44*, *Cp*, *Cxcl10*, *Lcn2*, *Serpina3n*, and *Gfap* (Figure 4a and Figure S2b).

The neuroinflammatory reactive astrocyte substate induced by microglial-derived factors TNF-α, IL-1α, and C1q can be recognized at the bulk sequencing level by the expression of *C3* and the upregulation of additional astrocyte gene transcripts (Hasel et al., 2021; Liddelow et al., 2017; Zamanian et al., 2012). Using qRT-PCR, we demonstrated significant upregulation of numerous gene transcripts associated with the astrocyte response to inflammation in astrocytes from injured WT mice (Figure 2a). When we performed the same qRT-PCR analysis on astrocytes isolated from TKO mice, nearly all

(12/14) of these significant changes in gene expression were no longer observed, indicating prevention of the astrocyte conversion to the *C3*-expressing neuroinflammatory substate (Figure 2a).

To understand if neuroinflammatory reactive astrocytes form within the affected white matter tracts in WMI and whether expression levels in this region specifically correlate with improved disease outcomes in TKO mice, we performed in situ hybridization for three transcripts associated with the neuroinflammatory reactive astrocyte substate. In situ hybridization for transcripts *C3* at 1 dpi revealed that approximately one-third of astrocytes in the injured WT corpus callosum express *C3* at 1 dpi compared with approximately 3% of astrocytes in the uninjured WT corpus callosum (Figure 4b,c and Figure S2a). The formation of these *C3*-expressing astrocytes was abrogated in TKO mice (Figure 4c). When we examined later timepoints after injury, we found that the proportion of astrocytes expressing *C3* remained significantly elevated in the injured relative to the uninjured corpus callosum at both 2 dpi and 9 dpi in WT mice (Figure 4d). Results for *C1s* and *Psmb8* followed the same pattern, with significant transcript

upregulation 24 h after injury in WT mice and no significant change in expression following injury in mutant mice (Figure 4e–h). Approximately, 50% of astrocytes express *Psmb8* in injured WT mice in comparison with only 5%–10% in uninjured mice.

3.4 | *C3*-expressing astrocytes form in human perinatal WMI

To determine whether the formation of *C3*-expressing neuroinflammatory reactive astrocytes is also a feature of human perinatal WMI, we obtained human postmortem brain tissue from infants affected by perinatal WMI and control cases matched as closely as possible based on gestational age at birth, age at time of death, and brain region. The diagnosis of WMI was determined postmortem by a neuropathologist. Both of the WMI cases that we examined involved preterm birth during the window of heightened preoligodendrocyte vulnerability between approximately 23 and 32 weeks gestation (Figure 5a). The infant we refer to as case 1 survived for only 12 days after birth, while the other infant (case 2) survived until 8 months of age, allowing us to assess the presence of *C3*-expressing astrocytes at both a short and a long time interval after injury (Figure 5a). Major clinical problems at the time of death for all four cases are summarized in Table S1. Using *C3* (ISH) and GFAP (IHC), we examined the proportion of GFAP positive astrocytes that also express *C3* in the white matter regions of this human tissue as well as in the same anatomical regions of the matched control cases. Over two-thirds (67%) of astrocytes in case 1 expressed *C3* in comparison with 5% in the control brain (Figure 5b–d). In case 2, one-third (33%) of astrocytes expressed *C3* in comparison with 5% in the control brain (Figure 5e).

4 | DISCUSSION

Significant progress has been made in recent years toward deciphering the spectrum of astrocyte reactivity in adult neurologic disease (Brandebura et al., 2023). In comparison, we know strikingly little about the astrocyte response to injury in the developing brain. Using a rodent model of perinatal WMI, we provide evidence, to our knowledge for the first time, for astrocyte conversion to a *C3*-expressing neuroinflammatory astrocyte substate in this disease. Using *C3* ISH, we were able to extend this finding to human postmortem brain tissue affected by WMI, confirming the relevance of this astrocyte conversion to human perinatal WMI.

Consistent with the notion of reactive astrocyte heterogeneity, only a subpopulation of astrocytes in the white matter regions we examined (30%–50% of astrocytes in mouse, 30%–60% of astrocytes in human) expressed the neuroinflammatory reactive astrocyte markers examined (*C3*, *C1s*, *Psmb8*) (Hasel et al., 2021). This proportion is comparable with the fraction of astrocytes expressing *C3* in other disease models, in which the abrogation of inflammatory astrocytes has been shown to improve disease outcomes; in these studies, C3 positive astrocytes accounted for 30%–60% of astrocytes in the

region of pathology (Guttenplan, Stafford et al., 2020; Guttenplan, Weigel et al., 2020; Yun et al., 2018).

Although our rodent WMI model involves a hypoxic insult in addition to an inflammatory insult, at the cell population level, we did not observe significant upregulation of the gene expression pattern formerly attributed to "A2" reactivity and initially described in association with ischemic injury (Figure S2c) (Liddelow et al., 2017; Zamanian et al., 2012). Without examining reactive astrocyte identity at the single cell level, the concomitant existence of astrocytes polarized in terms of gene expression in this direction cannot be excluded.

The formation of *C3*-expressing neuroinflammatory reactive astrocytes can be prevented by blocking the production of microglial-derived inflammatory molecules TNF-α, IL-1α, and C1q (Liddelow et al., 2017). In our mouse model of WMI, mutant mice lacking expression of these factors do not form *C3*-expressing neuroinflammatory reactive astrocytes and fail to develop the myelination defects and behavioral outcomes typical of WMI. While it is tempting to speculate that this reactive astrocyte substate may be playing a causal role in disease pathogenesis, the data presented to date only establish correlation between the presence of this reactive astrocyte substate and disease outcomes. While the data presented above suggest that neuronal death in cortical layers II/III is not likely a driving mechanism of disease in WMI, our experiments are inadequately powered to exclude this possibility. In contrast to our results in WT mice, we did not find significant change in microglial morphology following injury in TKO mice. This finding suggests that the microglial response to injury in these mice may be affected beyond failure to secrete TNF-α, IL-1α, and C1q, although gene expression studies of microglia in TKO mice following systemic inflammation indicate that these cells continue to upregulate other inflammatory mediators (Liddelow et al., 2017). Further work is needed to test whether neuroinflammatory reactive astrocytes are necessary and/or sufficient for the induction of WMI outcomes and to clarify the roles of other cell types.

Finally, fully understanding the landscape of astrocyte reactivity and its functional implications in any disease state ultimately requires gene expression analysis at single cell resolution, data on the spatial coordinates of gene expression, and extensive experimental studies using in vitro modeling and manipulation of gene expression to uncover the functional consequences of these transcriptomically-defined reactive substates. Using these tools, it will be fascinating to uncover unique properties of astrocyte reactivity in response to the combined inflammatory/hypoxic injury of WMI and to elucidate differences in astrocyte responses to injury in the perinatal versus adult brain.

CONFLICT OF INTEREST STATEMENT

SL maintains a financial interest in AstronauTx Ltd, UK, who were not funders of this study. Other funders had no role in the design of the study; in the collection, analyses, or interpretation of data; in the writing of the manuscript; or in the decision to publish the results. Other authors of this study have no conflicts of interest to disclose.

DATA AVAILABILITY STATEMENT

The data that support the findings of this study are available from the corresponding author upon reasonable request.

ORCID

Valérie Haesler https://orcid.org/0000-0001-8470-0052
Vera Tscherrig https://orcid.org/0000-0002-3601-5453
Manideep Chavali https://orcid.org/0000-0002-0580-103X
Shane Liddelow https://orcid.org/0000-0002-0840-1437
David H. Rowitch https://orcid.org/0000-0002-0079-0060
Daniel Surbek https://orcid.org/0000-0001-7705-1584
Andreina Schoeberlein https://orcid.org/0000-0002-6716-9551
Amanda Brosius Lutz https://orcid.org/0000-0001-6227-104X

REFERENCES

Back, S. A. (2017). White matter injury in the preterm infant: Pathology and mechanisms. *Acta Neuropathologica*, 134(3), 331–349.

Ben Haim, L., & Rowitch, D. H. (2017). Functional diversity of astrocytes in neural circuit regulation. *Nature Reviews Neuroscience*, 18(1), 31–41.

Brandebura, A. N., Paumier, A., Onur, T. S., & Allen, N. J. (2023). Astrocyte contribution to dysfunction, risk and progression in neurodegenerative disorders. *Nature Reviews. Neuroscience*, 24(1), 23–39.

Eggenberger, S., Boucard, C., Schoeberlein, A., Guzman, R., Limacher, A., Surbek, D., & Mueller, M. (2019). Stem cell treatment and cerebral palsy: Systemic review and meta-analysis. *World journal of Stem Cells*, 11(10), 891–903.

Foo, L. C., Allen, N. J., Bushong, E. A., Ventura, P. B., Chung, W. S., Zhou, L., Cahoy, J. D., Daneman, R., Zong, H., Ellisman, M. H., & Barres, B. A. (2011). Development of a method for the purification and culture of rodent astrocytes. *Neuron*, 71(5), 799–811.

Guttenplan, K. A., Stafford, B. K., El-Danaf, R. N., Adler, D. I., Münch, A. E., Weigel, M. K., Huberman, A. D., & Liddelow, S. A. (2020). Neurotoxic reactive astrocytes drive neuronal death after retinal injury. *Cell Reports*, 31(12), 107776.

Guttenplan, K. A., Weigel, M. K., Adler, D. I., Couthouis, J., Liddelow, S. A., Gitler, A. D., & Barres, B. A. (2020). Knockout of reactive astrocyte activating factors slows disease progression in an ALS mouse model. *Nature Communications*, 11(1), 3753.

Guttenplan, K. A., Weigel, M. K., Prakash, P., Wijewardhane, P. R., Hasel, P., Rufen-Blanchette, U., Münch, A. E., Blum, J. A., Fine, J., Neal, M. C., Bruce, K. D., Gitler, A. D., Chopra, G., Liddelow, S. A., & Barres, B. A. (2021). Neurotoxic reactive astrocytes induce cell death via saturated lipids. *Nature*, 599(7883), 102–107.

Hasel, P., Rose, I. V. L., Sadick, J. S., Kim, R. D., & Liddelow, S. A. (2021). Neuroinflammatory astrocyte subtypes in the mouse brain. *Nature Neuroscience*, 24(10), 1475–1487.

Khakh, B. S., & Sofroniew, M. V. (2015). Diversity of astrocyte functions and phenotypes in neural circuits. *Nature Neuroscience*, 18(7), 942–952.

Liddelow, S. A., Guttenplan, K. A., Clarke, L. E., Bennett, F. C., Bohlen, C. J., Schirmer, L., Bennett, M. L., Münch, A. E., Chung, W. S., Peterson, T. C., Wilton, D. K., Frouin, A., Napier, B. A., Panicker, N., Kumar, M., Buckwalter, M. S., Rowitch, D. H., Dawson, V. L., Dawson, T. M., … Barres, B. A. (2017). Neurotoxic reactive astrocytes are induced by activated microglia. *Nature*, 541(7638), 481–487.

Nobuta, H., Ghiani, C. A., Paez, P. M., Spreuer, V., Dong, H., Korsak, R. A., Manukyan, A., Li, J., Vinters, H. V., Huang, E. J., Rowitch, D. H., Sofroniew, M. V., Campagnoni, A. T., de Vellis, J., & Waschek, J. A. (2012). STAT3-mediated astrogliosis protects myelin development in neonatal brain injury. *Annals of Neurology*, 72(5), 750–765.

Renz, P., Schoeberlein, A., Haesler, V., Maragkou, T., Surbek, D., & Brosius, L. A. (2022). A novel murine multi-hit model of perinatal acute diffuse white matter injury recapitulates major features of human disease. *Biomedicines*, 10(11), 2810.

Shiow, L. R., Favrais, G., Schirmer, L., Schang, A. L., Cipriani, S., Andres, C., Wright, J. N., Nobuta, H., Fleiss, B., Gressens, P., & Rowitch, D. H. (2017). Reactive astrocyte COX2-PGE2 production inhibits oligodendrocyte maturation in neonatal white matter injury. *Glia*, 65(12), 2024–2037.

Srivastava, T., Sherman, L. S., & Back, S. A. (2020). Dysregulation of Hyaluronan homeostasis during white matter injury. *Neurochemical Research*, 45(3), 672–683.

Thomi, G., Surbek, D., Haesler, V., Joerger-Messerli, M., & Schoeberlein, A. (2019). Exosomes derived from umbilical cord mesenchymal stem cells reduce microglia-mediated neuroinflammation in perinatal brain injury. *Stem Cell Research & Therapy*, 10(1), 105.

Volpe, J. J. (2019). Dysmaturation of premature brain: Importance, cellular mechanisms, and potential interventions. *Pediatric Neurology*, 95, 42–66.

Wheeler, M. A., Jaronen, M., Covacu, R., Zandee, S. E. J., Scalisi, G., Rothhammer, V., Tjon, E. C., Chao, C. C., Kenison, J. E., Blain, M., Rao, V. T. S., Hewson, P., Barroso, A., Gutiérrez-Vázquez, C., Prat, A., Antel, J. P., Hauser, R., & Quintana, F. J. (2019). Environmental control of astrocyte pathogenic activities in CNS inflammation. *Cell*, 176(3), 581–596.e18.

Yun, S. P., Kam, T. I., Panicker, N., Kim, S. M., Oh, Y., Park, J. S., Kwon, S. H., Park, Y. J., Karuppagounder, S. S., Park, H., Kim, S., Oh, N., Kim, N. A., Lee, S., Brahmachari, S., Mao, X., Lee, J. H., Kumar, M., An, D., … Ko, H. S. (2018). Block of A1 astrocyte conversion by microglia is neuroprotective in models of Parkinson's disease. *Nature Medicine*, 24(7), 931–938.

Zamanian, J. L., Xu, L., Foo, L. C., Nouri, N., Zhou, L., Giffard, R. G., & Barres, B. A. (2012). Genomic analysis of reactive astrogliosis. *The Journal of Neuroscience, 32*(18), 6391–6410.

SUPPORTING INFORMATION

Additional supporting information can be found online in the Supporting Information section at the end of this article.